Lagrangian coherent structures in low Reynolds number swimming

Lagrangian coherent structures in low Reynolds number swimming

Megan M Wilson[1]**, Jifeng Peng**[2]**, John O Dabiri**[2,3] **and Jeff D Eldredge**[1]

[1] Mechanical and Aerospace Engineering Department, University of California Los Angeles,
Los Angeles, CA 90095, USA
[2] Department of Bioengineering, California Institute of Technology, Pasadena,
CA 91125, USA
[3] Graduate Aeronautical Laboratories, California Institute of Technology,
Pasadena, CA 91125, USA

Abstract

This work explores the utility of the finite-time Lyapunov exponent (FTLE) field for revealing flow structures in low Reynolds number biological locomotion. Previous studies of high Reynolds number unsteady flows have demonstrated that ridges of the FTLE field coincide with transport barriers within the flow, which are not shown by a more classical quantity such as vorticity. In low Reynolds number locomotion (O(1)–O(100)), in which viscous diffusion rapidly smears the vorticity in the wake, the FTLE field has the potential to add new insight to locomotion mechanics. The target of study is an articulated two-dimensional model for jellyfish-like locomotion, with swimming Reynolds number of order 1. The self-propulsion of the model is numerically simulated with a viscous vortex particle method, using kinematics adapted from previous experimental measurements on a live medusan swimmer. The roles of the ridges of the computed forward- and backward-time FTLE fields are clarified by tracking clusters of particles both backward and forward in time. It is shown that a series of ridges in front of the jellyfish in the forward-time FTLE field transport slender fingers of fluid toward the lip of the bell orifice, which are pulled once per contraction cycle into the wake of the jellyfish, where the fluid remains partitioned. A strong ridge in the backward-time FTLE field reveals a persistent barrier between fluid inside and outside the subumbrellar cavity. The system is also analyzed in a body-fixed frame subject to a steady free stream, and the FTLE field is used to highlight differences in these frames of reference.

(Some figures in this article are in colour only in the electronic version)

1. Introduction

Fluid mechanical studies of animal swimming typically focus on the Eulerian velocity and vorticity fields created by the animals. In recent years, a new approach has been developed that studies animal swimming from a Lagrangian perspective [1–3]. The premise of this method is to consider the fluid as a dynamical system of fluid particles rather than a continuum. By following the trajectories of an ensemble of fluid particles, calculated from velocity fields or directly measured from experiments, Lagrangian coherent structures (LCS) are observed to separate the fluid into regions with distinct dynamics [4]. LCS act as transport barriers in the flow. Therefore they can efficiently describe the entire fluid transport geometry. Since the LCS are generally not shown by classical quantities such as velocity or vorticity, their evolution provides a unique tool to study mass and momentum transport.

To date, the Lagrangian approach has only been applied to animals swimming at relatively large Reynolds numbers (O(1000)), e.g. adult moon jellyfish and bluegill sunfish [1–3]. Non-biological applications of the method have been pursued at Reynolds number of the same order of magnitude or higher [3, 5, 6]. The method itself is independent of Reynolds number because the analysis is based solely on flow kinematics, i.e. Lagrangian fluid particle trajectories. Hence, application to low Reynolds number swimming has the potential to add new insight to locomotion mechanics in
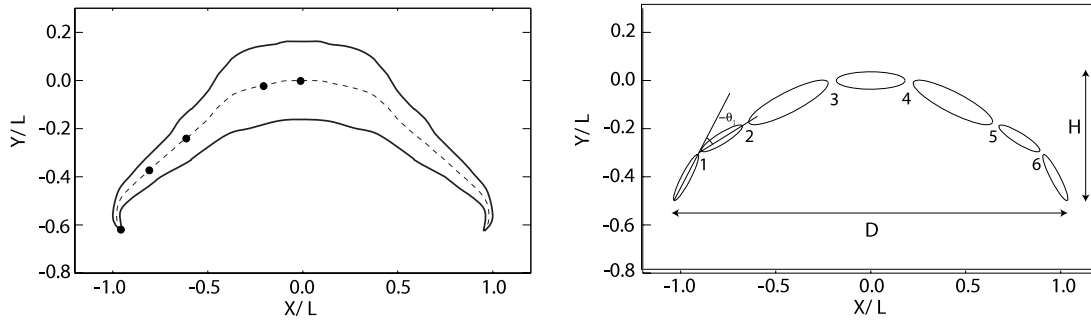
Figure 1. Simplified jellyfish kinematic model: (*left*) projected outline and centerline of the jellyfish from experimental data [7], with marker points (●) used for generating articulated model; (*right*) articulated system of linked rigid bodies and numbering system used for hinges. H and D denote the height and diameter of the model, respectively.
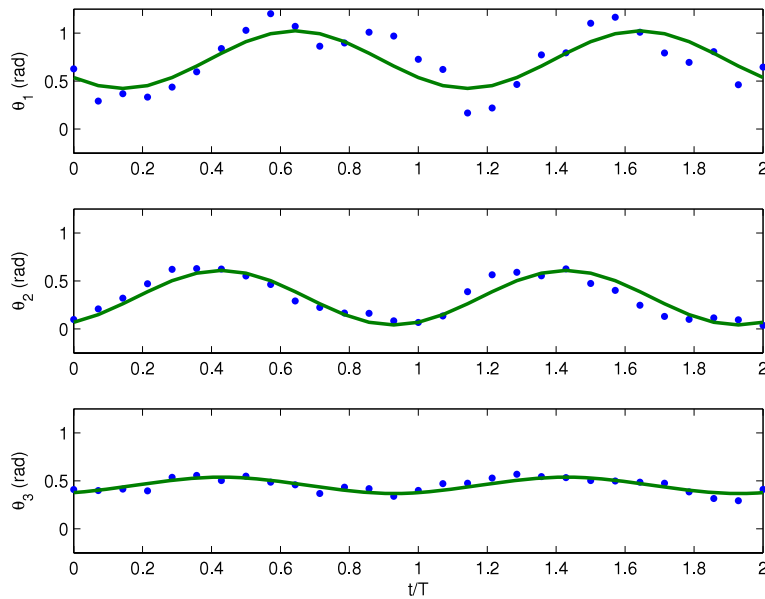

Figure 2. Measured angles (circles) and sinusoidal hinge correlations for hinges 1–3.

this regime, especially given that existing Eulerian metrics (e.g. vorticity) are largely obscured by diffusion.

In the present study, we apply the LCS method to a jellyfish-like model swimming at low Reynolds number (O(1)–O(100)). During early stages of their life cycle, jellyfish ephyrae (larva) swim at low Reynolds number due to their small size and low cruising speed. Only after they are fully developed do jellyfish medusae (adults) swim at high Reynolds number. Thus the present model, while an abstraction, is useful for understanding the challenges faced by real animals in viscous environments. The LCS analysis illustrates the mechanism of advective transport and quantifies the limitations of advective transport at low Reynolds numbers.

The paper is organized as follows. Section 2 describes the target problem and the model. This is followed by a presentation of the numerical simulation methodology and the calculation of FTLE and LCS in section 3. Section 4 reports results obtained from the analysis. The FTLE of the flow generated by the jellyfish is presented and a detailed description of fluid particle advection is given to add physical intuition to the FTLE results. The paper concludes with a brief summary in section 5.

2. Target problem

The target of this study is a two-dimensional jellyfish-like model, consisting of an articulated system of seven linked rigid bodies, shown in figure 1. As this figure depicts schematically, the rigid-body system approximates the centerline of the projected outline of an oblate medusan jellyfish [2, 7]. The motion of this centerline was reconstructed from a sequence of snapshots of the outline, obtained from filming the rectilinear swimming of this jellyfish over two contraction cycles. Five marker points on one side of the centerline, as shown in the left panel of figure 1, were tracked over this interval, and the secants joining these points were used to divide the centerline into discrete links. The angles between these secants are plotted for the left side of the body in figure 2. Each of the angle time sequences was fitted with a sinusoid, as shown in this figure, and the resulting functions were used to prescribe the angles of hinges between the rigid bodies. The constituent bodies are each rigid ellipses with length equal to the mean length of the corresponding secant and with density equal to the surrounding fluid. The kinematics and system are both left–right symmetric.
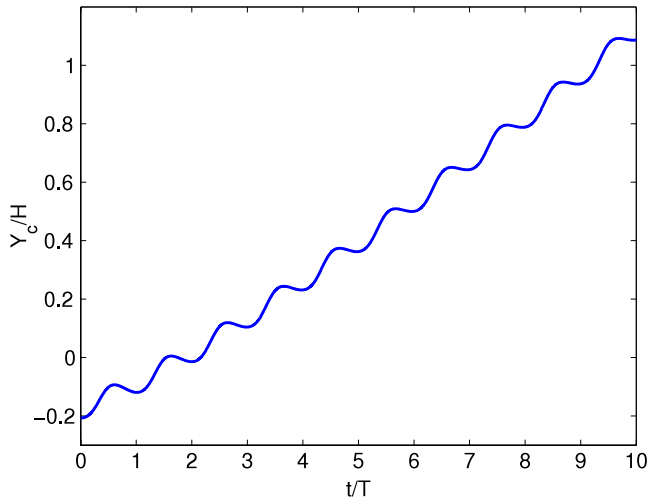
Figure 3. Longitudinal position, $Y_c/\overline{H}$, of the centroid of the self-propelling jellyfish.

Figure 4. Longitudinal velocity, $V_c T/\overline{H}$, of the jellyfish centroid. The mean velocity was found to be $\overline{V}_c T/\overline{H} \approx 0.16$.

It is important to emphasize that this simple model is only meant to serve as an abstraction of jellyfish locomotion. In particular, three-dimensional phenomena such as vortex stretching, which likely influence the mechanics of a biological swimmer, are clearly missing from this model. No attempt was made to account for the thickness of the actual organism, as is evident in figure 1. The gaps between bodies, which are transparent to the flow, are included in order to simplify the numerics. Though it is possible to wrap a 'skin' around the system, it was decided that such a feature was unnecessary within the scope of this study.

Figure 1 depicts three length scales. The coordinates are scaled by L, which denotes the arc length from the lip of the jellyfish orifice to the innermost hinge (hinge 3). The shape changes also give rise to two other length scales: $\overline{H}$, the mean 'height' of the bell, and $D_{\max}$, the maximum diameter of the bell. The ratios of these length scales are $\overline{H}/L \approx 0.67$ and $D_{\max}/L \approx 2.1$. The undulation period, T, forms a natural timescale for the problem. The prescribed hinge kinematics give rise to the largest speed at the orifice lip, which, relative to the centroid of the frontmost body, is $|U_{\text{lip}}|_{\max} \approx 1.5L/T$.

There are two relevant Reynolds numbers in this problem, one based on the kinematics and another based on the resulting self-propulsion. The kinematic Reynolds number, Re_k, defined here based on $|U_{\text{lip}}|_{\max}$ and $\overline{H}$, is set throughout the simulations at $\text{Re}_k = |U_{\text{lip}}|_{\max}\overline{H}/\nu = 16$, where ν is the kinematic viscosity. (It is also useful to note a slightly different definition, based on maximum bell diameter and the undulation period: $Re_{k2} = D_{\max}^2/T\nu$. Its value is approximately 69 here, while in the larger jellyfish medusae studied by Dabiri *et al* [7], the value was approximately 4700. The present regime is characteristic of a jellyfish larva, however.) The propulsion Reynolds number, $\text{Re}_p = \overline{V}_c H/\nu$, based on the mean longitudinal speed $\overline{V}_c$ of the centroid of the jellyfish and the mean height $\overline{H}$, is determined during the course of the simulation.
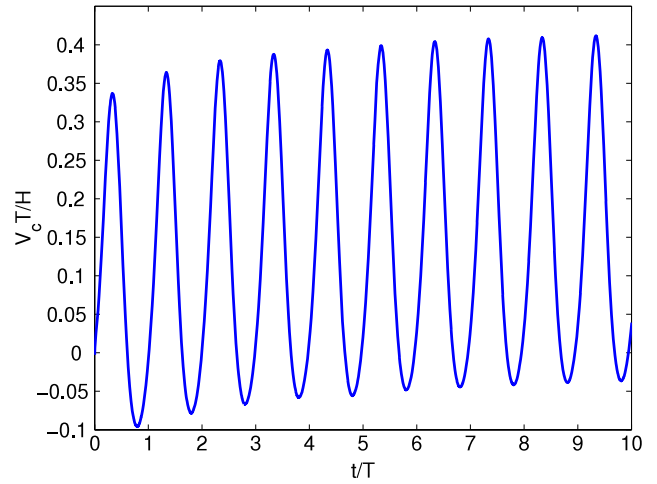
3. Methodology

3.1. Numerical method

The numerical simulations were carried out with a viscous vortex particle method, with strong coupling to the body dynamics. This high-fidelity method solves the Navier–Stokes equations by means of vorticity-bearing computational particles; the particles move with the local velocity field, and exchange strength to account for viscous diffusion. The dynamical coupling with the body and the enforcement of kinematic boundary conditions are handled simultaneously, through the flux of new vorticity to nearby particles and the update of body position and velocity via Newton's second law. The moving particles provide the method with a natural adaptivity to the changing body configuration. Furthermore, particles are only needed in regions in which vorticity is non-zero. The reader is referred to previous work for details of the methodology [8, 9].

3.2. Computation of the finite-time Lyapunov exponent (FTLE) field

The theoretical foundation of the finite-time Lyapunov exponent field has been discussed in detail in previous papers (see, for example [4, 5]), and the interested reader is referred to these for guidance. Here, we focus primarily on the computation of the FTLE field, which differs in some respects from previous studies. Indeed, by obtaining the velocity field through the Biot–Savart induction of vorticity-bearing particles, the vortex particle method provides somewhat more direct access to the FTLE field than a grid-based method. In particular, the velocity gradient tensor field is itself induced by the particles, and this fact is used to avoid finite differencing of the particle map and the associated noise this procedure introduces.

Consider the particle trajectories given by solution of the equation

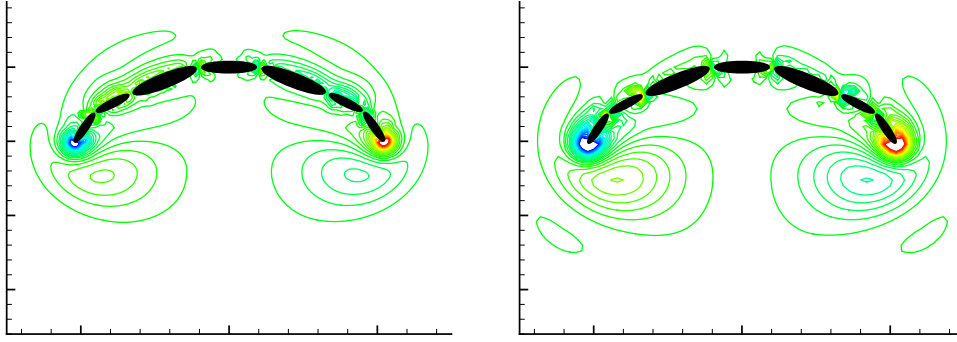$$\frac{\mathrm{d}\boldsymbol{X}}{\mathrm{d}t} = \boldsymbol{v}[\boldsymbol{X}(t; t_0, \boldsymbol{x}_0), t], \tag{1}$$

Figure 5. Vorticity field: free swimming (*left*), fixed swimming (*right*). The contour levels of vorticity are identical.

$$X(t_0; t_0, x_0) = x_0. \qquad (2)$$

The flow map, $\phi_{t_0}^t$, represents the solution of this equation for fixed initial time, t_0; it maps particles to their final position at time t:

$$\phi_{t_0}^t : x_0 \mapsto \phi_{t_0}^t(x_0) = X(t; t_0, x_0). \qquad (3)$$

Formally, this flow map is written as the time integral of the velocity field,

$$\phi_{t_0}^t(x_0) = X(t; t_0, x_0) = x_0 + \int_{t_0}^t v[X(\tau; t_0, x_0), \tau]\, \mathrm{d}\tau. \qquad (4)$$

The Jacobian of this flow map is its derivative with respect to changes in the initial particle location. This derivative can be applied to the integral in (4) to obtain the expression

$$\frac{\mathrm{d}\phi_{t_0}^t}{\mathrm{d}x}(x_0) = I + \int_{t_0}^t \frac{\mathrm{d}\phi_{t_0}^\tau}{\mathrm{d}x}(x_0) \cdot \nabla v[X(\tau; t_0, x_0), \tau]\, \mathrm{d}\tau. \qquad (5)$$

Through this equation, the deformation experienced between nearby points arises from the cumulative action of the velocity gradient tensor. Note that the Jacobian between the initial and final configuration of the flow depends on its complete history during the interval.

The finite-time version of the (right) Cauchy–Green deformation tensor, Δ, at a given point x is defined by

$$\Delta(x) = \left(\frac{\mathrm{d}\phi_t^{t+T_{\mathrm{LE}}}}{\mathrm{d}x}(x)\right)^* \frac{\mathrm{d}\phi_t^{t+T_{\mathrm{LE}}}}{\mathrm{d}x}(x), \qquad (6)$$

where $()^*$ denotes the transpose of the tensor. So defined, the tensor quantifies the stretching of an infinitesimal material line over the interval $[t, t + T_{\mathrm{LE}}]$. The maximum eigenvalue, $\lambda_{\max}$, of this tensor represents the maximum stretching that will occur near x over this interval, when the material line is aligned with the corresponding eigenvector. This eigenvalue constitutes the FTLE field, $\sigma_{t_0}^{T_{\mathrm{LE}}}$, defined as

$$\sigma_{t_0}^{T_{\mathrm{LE}}}(x) = \frac{1}{|T_{\mathrm{LE}}|} \ln \sqrt{\lambda_{\max}(\Delta(x))}. \qquad (7)$$

The forward-time FTLE field, when $T_{\mathrm{LE}} > 0$, is constructed to reveal repelling Lagrangian coherent structures (LCS), which are analogous to stable manifolds in a steady flow (see, e.g., [4]). In contrast, setting $T_{\mathrm{LE}} < 0$ leads to the
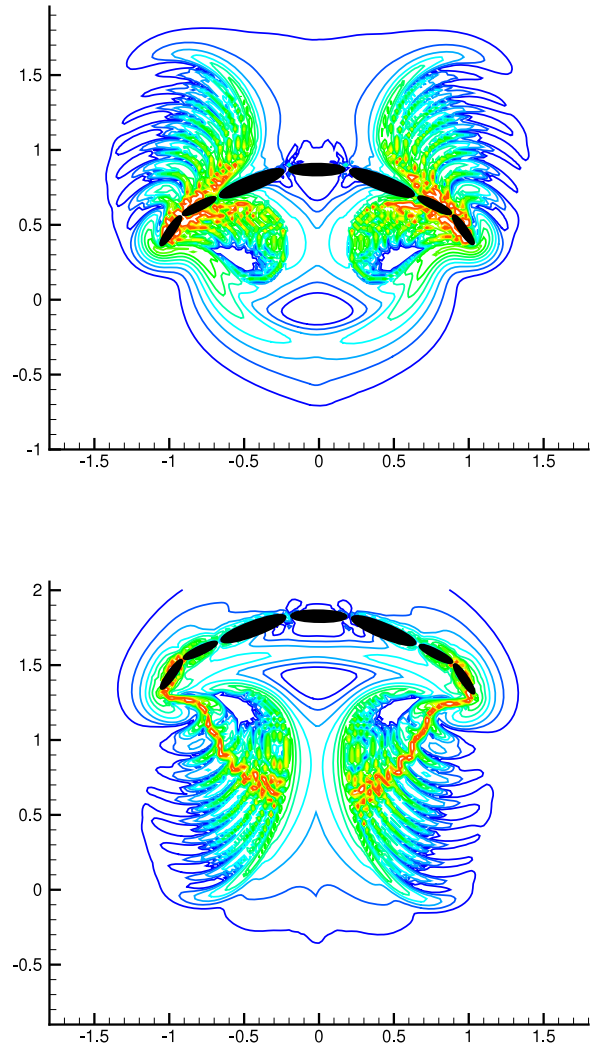

Figure 6. For free-swimming locomotion: (*top*) forward-time FTLE field, at $t/T = 10$, using $T_{\mathrm{LE}} = 9T$; (*bottom*) backward-time FTLE field at $t/T = 19$, with $T_{\mathrm{LE}} = -9T$. Red corresponds to largest magnitude, while blue is smallest.

backward-time FTLE field, in which attracting LCS (analogous to unstable manifolds) are uncovered.

The usual technique for computing (7) is based on velocity data (obtained experimentally or from grid-based simulation) that is only available at fixed grid points. In such cases,
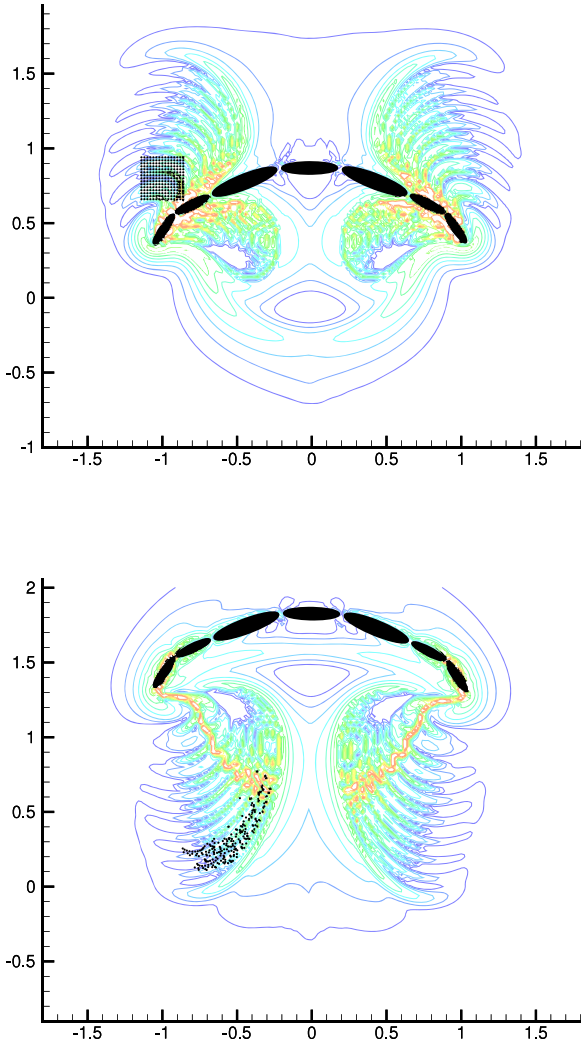
Figure 7. (*Top*) Forward-time FTLE field and initial block of tracer particles (black circles) at $t/T = 10$; (*bottom*) backward-time FTLE field and final configuration of tracer particles at $t/T = 19$.

Figure 8. (*Top*) Forward-time FTLE field and initial configuration of tracer particles (black circles) at $t/T = 10$; (*bottom*) backward-time FTLE field and final configuration of tracer particles at $t/T = 19$.
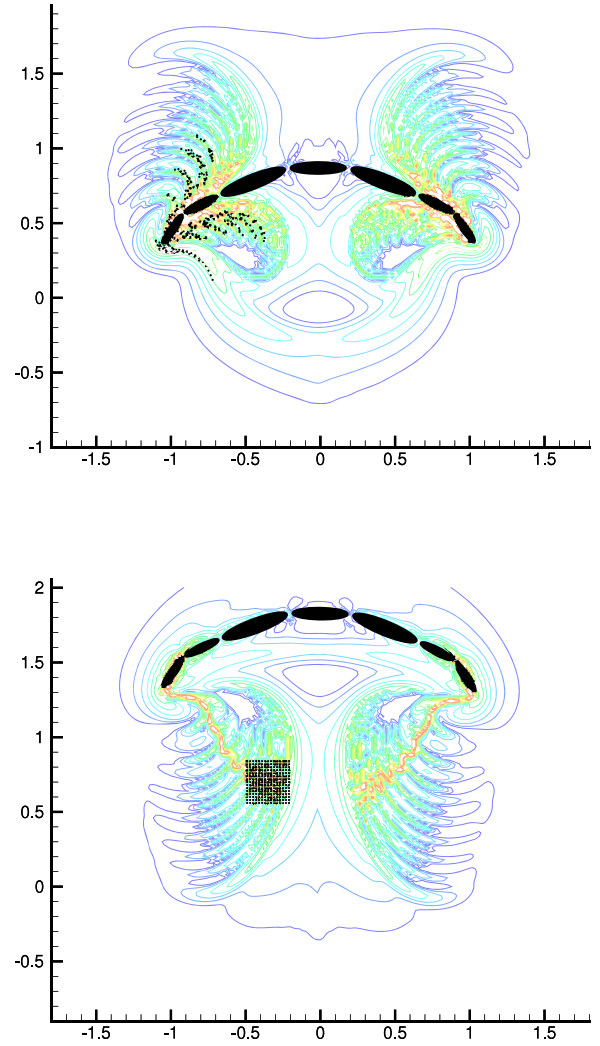
the data must be interpolated at the locations of advecting particles, and the spatial gradient of the resulting flow map obtained by finite differencing at the grid points from which the particles were launched. The approach taken here is different, in that equations (4) and (5) are used in tandem to compute the Jacobian along the trajectories of a set of advecting particles.

The data from a vortex particle simulation consist of the instantaneous locations and vortex strengths of the computational particles. These data determine not only the entire velocity field, but also its spatial gradient. Consider, for example, a single vortex particle at the origin, with its accompanying strength Γ. It carries a smooth vorticity distribution with radius ε,

$$\omega(\boldsymbol{x}) = \frac{\Gamma}{\varepsilon^2} \zeta(|\boldsymbol{x}|/\varepsilon), \tag{8}$$

where ζ is the regularization function (in this work, $\zeta(r) = \exp(-r^2)/\pi$). This particle 'induces' a planar velocity field

given by

$$\boldsymbol{v}(\boldsymbol{x}) = \frac{\Gamma}{2\pi |\boldsymbol{x}|^2} \begin{pmatrix} -y \\ x \end{pmatrix} q(|\boldsymbol{x}|/\varepsilon), \tag{9}$$

where $\boldsymbol{x} = (x, y)$, and q represents the de-singularization provided by the smooth particle:

$$q(r) = 2\pi \int_0^r r' \zeta(r') \, \mathrm{d}r. \tag{10}$$

In turn, the velocity gradient field corresponding to the vortex particle is obtained by differentiating (9) [10]:

$$\nabla \boldsymbol{v}(\boldsymbol{x}) = -\Gamma \frac{\zeta(|\boldsymbol{x}|/\varepsilon)}{\varepsilon^2 |\boldsymbol{x}|^2} \begin{bmatrix} xy & y^2 \\ -x^2 & -xy \end{bmatrix}$$
$$+ \frac{\Gamma}{2\pi} \frac{q(|\boldsymbol{x}|/\varepsilon)}{|\boldsymbol{x}|^4} \begin{bmatrix} 2xy & y^2 - x^2 \\ y^2 - x^2 & -2xy \end{bmatrix}. \tag{11}$$

Thus, the velocity gradient at any point (inside or outside the region of particle coverage) is provided by the collective influence of all such smooth vortex particles. This enables a more spatially extended computation of the FTLE field, when desired.
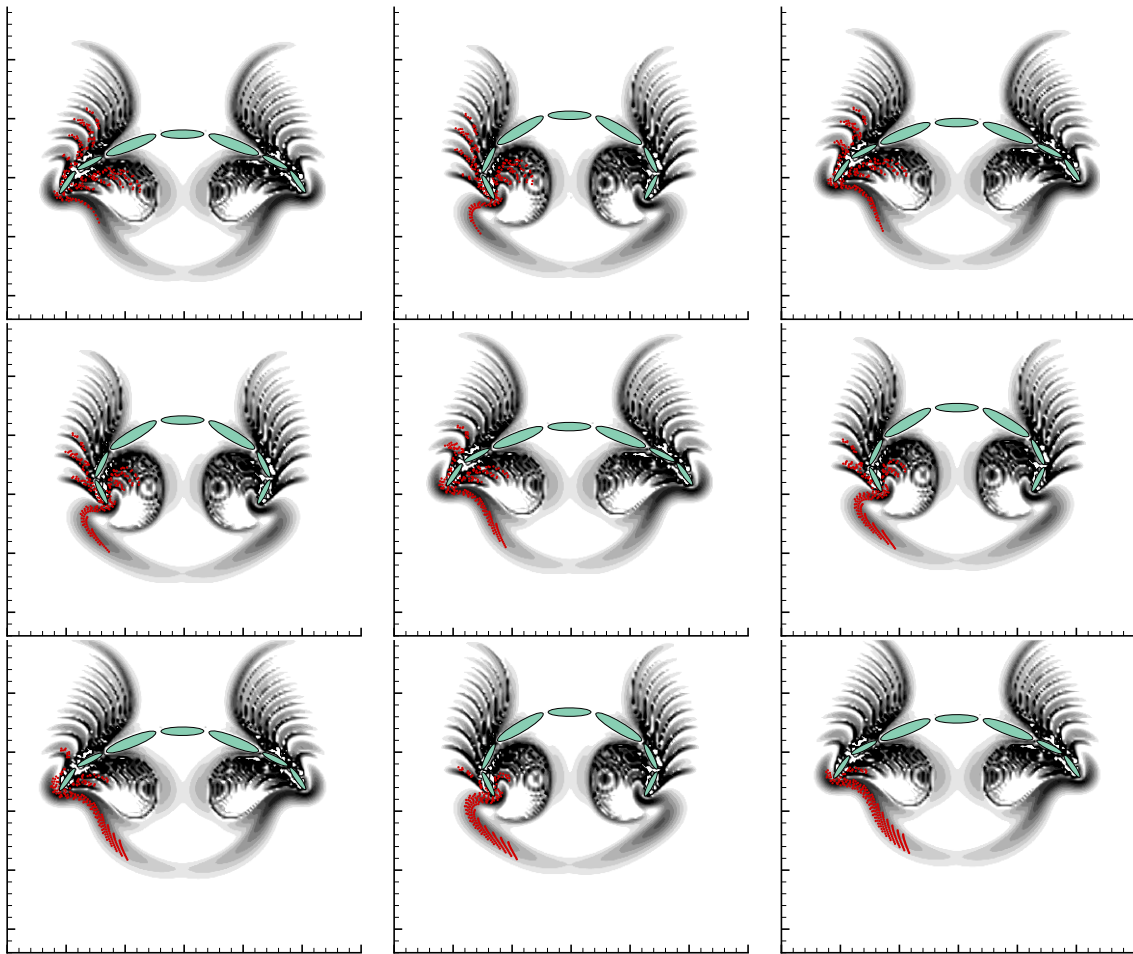
Figure 9. Snapshots from $t/T = 10$ to 14 in increments of $0.5T$, from left to right then top to bottom, of the forward-time FTLE and corresponding configuration of the backward-tracked block of particles in figure 8. The particles are depicted in red.

One is tempted to unify the entire vortex method/FTLE procedure by identifying the FTLE particles with those particles already used for the Navier–Stokes simulation. However, these latter particles lose their identity every few time steps, as they must be occasionally re-initialized to a new set to preserve the accuracy of the method [8, 11]. Consequently, the FTLE computation procedure is carried out in post-processing, using a distinct set of particles that covers the region of interest. These FTLE particles are initially situated on a uniform grid, with spacing an integer multiple of the initial spacing of the vortex particles (for the results presented here, a factor of two is used).

4. Results

The jellyfish model was simulated in self-propulsion, starting from rest in a stationary fluid. For all simulations reported in this work, the particle spacing was $0.01L$ and the time-step size was $8 \times 10^{-4}T$. It was verified that these choices led to sufficiently converged simulation results. The resulting longitudinal position and velocity of the centroid of the jellyfish over the first ten periods are shown in figures 3 and 4, respectively. It was necessary to run the simulation for at least

six periods in order for the mean velocity to become stationary; the resulting mean was found to be $\overline{V}_c T/H \approx 0.16$. In other words, the system requires 6.4 contractions in order to travel one body height. Thus, the propulsion Reynolds number, as defined in section 2, is approximately 1.1.

In studies of biological mechanisms of locomotion, it is common to adopt a frame of reference in which the creature is tethered in a constant and uniform free stream. The speed of this free stream is adjusted so that the mean longitudinal force exerted on the creature vanishes. However, such a reference frame omits the possibly important variations in speed of a freely-swimming creature, as clearly exhibited in figure 4. In order to identify differences between these reference frames, a tethered model was also simulated. The prescribed kinematics were identical to those from the self-propelling case. However, the head of the tethered model was held fixed in space, and the system was subjected to a free stream with velocity equal and opposite to the mean forward velocity of the self-propelling case (for which the mean longitudinal force vanishes).

4.1. Vorticity field

The instantaneous vorticity fields generated by both the free-swimming and fixed jellyfish at the same point in their cycles

are depicted in figure 5. Both cases exhibit features that are consistent with previous studies of live jellyfish swimming [7]. At the instant shown, the bell is beginning its contraction phase, and the seed of a starting vortex is apparent at each lip of the orifice. Meanwhile, a fully-developed pair of stopping vortices persist in the wake of the bell. Due to the much lower Reynolds number, these vortices diffuse much more rapidly than in the previous experimental studies, preventing an extensive vortical wake from developing behind the jellyfish.

The side-by-side comparison between the free-swimming and tethered models illustrates only small differences in the vorticity field. In particular, the strength of the stopping and starting vortices are slightly stronger in the fixed swimmer. However, it is difficult to distinguish differences between these two flows by simply by comparing vorticity. The FTLE field will be used in section 4.4 to highlight these differences more clearly.

4.2. Forward- and backward-time FTLE fields

Data from the numerical simulation for the free-swimming case was used to compute the FTLE field with the method described in section 3.2. All of the FTLE analysis was performed with particles uniformly spaced $0.02L$ units apart, and with forward Euler time-marching with a step size of $0.019T$. Figure 6 depicts the forward- and backward-time FTLE fields at times $t/T = 10$ and 19, respectively. The particle trajectories and their Jacobians are integrated over intervals of duration $T_{LE} = 9T$ and $-9T$, respectively. These integration times were chosen purposefully to reveal as much structure in the flow as possible. Note that the backward-time field is shown at the end of the integration interval for the forward-time field, and vice versa.

The forward-time FTLE field at $t/T = 10$ consists of a sequence of nine curved ridges on the left and right sides in the front of the jellyfish. A weaker ridge sits between each pair of these nine dominant ones, and the entire series is rooted at the outside of the orifice lip. The ridges nearer to the axis of symmetry are narrower and more elongated; the final ridges are, in fact, nearly indistinguishable. A similar sequence of ridges is found inside the subumbrellar cavity, though its structure is less clearly resolved. The last of these interior ridges appears to enclose the entire sequence. Finally, a single weak ridge extends downward from either lip and—together with the body itself—envelops the cavity.

The backward-time FTLE field at $t/T = 19$ is also characterized by a sequence of nine ridges, which each extend orthogonally and downward (and a companion sequence extends, less clearly, upward) from a strong corrugated ridge attached to each lip of the orifice. As in the forward-time FTLE field, the ridges in the sequence that are nearer the axis of symmetry are narrower and more elongated. The most central ridge nearly envelops the region just above the corrugated dividing ridge.

Though the ridges identified in both of these fields are distinct, the role that they play in fluid transport is not clear. In the next section, they are interpreted by means of particle tracking.
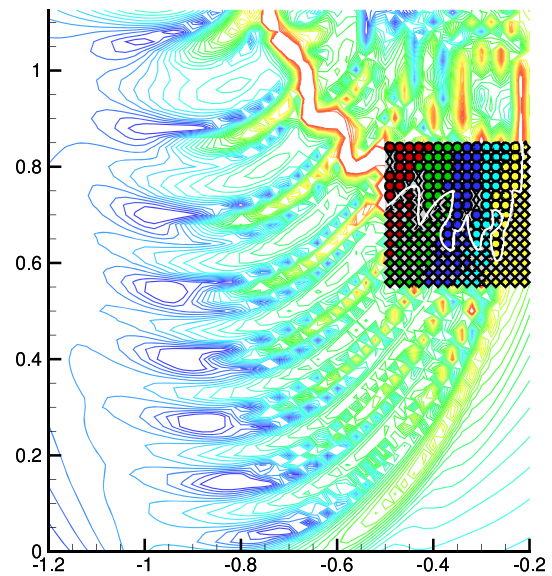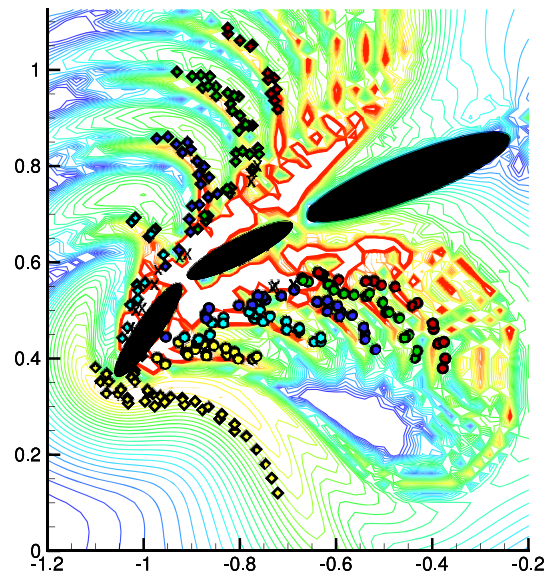

Figure 10. (*Top*) Initial locations of tagged particles overlaid on the forward-time FTLE field $t/T = 10$; (*bottom*) final configuration of tagged particles overlaid on backward-time FTLE field at $t/T = 19$.

4.3. Particle evolution

Tracer particles were introduced in small clusters in order to provide a physical interpretation of the FTLE ridges. In the first case, a square block of particles was released just outside of the orifice lip, as shown in figure 7. The block initially overlaps several ridges in the sequence in the forward-time FTLE field at the same instant of the release of particles ($t/T = 10$). After nine periods, the particles appear to align with the elongated ridges shown in the backward-time FTLE field computed at the same instant.

Another particle block was placed below the jellyfish bell at $t/T = 19$ and tracked backward in time to $t/T = 10$, as shown in figure 8. The final placement of the block of particles was chosen so that it overlapped the strong corrugated
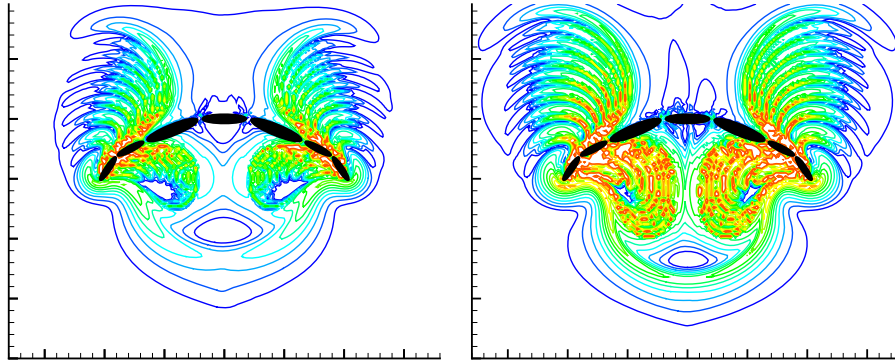
Figure 11. Forward-time FTLE field for: self-propelled swimmer (*left*) and tethered system (*right*). The same contour levels are used for both plots.
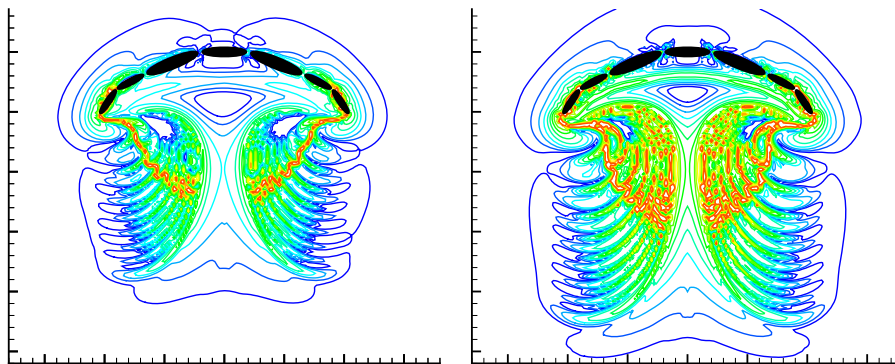

Figure 12. Backward-time FTLE field for: self-propelled swimmer (*left*) and tethered system (*right*). The same contour levels are used for both plots.

ridge below the bell in the backward-time FTLE field. After backward-time tracking, these particles appear to align with both the interior and exterior sequences of ridges shown in the forward-time FTLE field at $t/T = 10$.

The evolution of these particles and of the corresponding forward-time FTLE field is shown in figure 9 from $t/T = 10$ to 14 in half-period increments. Making use of the periodicity of the flow, each FTLE field between $t/T = 11$ and 14 was generated by translating the fields at $t/T = 10$ and 10.5 upward by the corresponding distance of travel of the fish. In half of one cycle, the structure of the FTLE field does not change, though the ridges deform in response to the bell contraction, and each ridge in the series of nine is pulled closer to the lip. Particles are trapped between neighboring ridges. As the bell expands to complete the cycle, the interior and exterior ridges nearest the lip coalesce with the U-shaped structure that spans the region below the bell; the particles aligned with these ridges slide down this structure. Meanwhile each remaining ridge has taken the place of the one it preceded. The process repeats in each contraction cycle, until all threads of particles have been pulled down the U-shaped structure into the wake of the jellyfish.

To further elucidate this process, the particles in their early (deformed) configuration were manually tagged according to the finger-like zone that they inhabit, as shown in the upper plot in figure 10. Particles marked with an X were unable to be placed into a specific set with confidence. The final configuration of the distinctly tagged particles is shown in the lower plot of figure 10. Each set of particles also forms a distinct group in its final position, and the borders between these groups appear to coincide with the ridges in the backward-time FTLE field. The sequence of particle threads is also preserved in the final groupings: particles in the thread extending downward from the lip at $t/T = 10$ (the yellow diamonds) eventually comprise the innermost group at the final time; each successive thread pulled from the lip region, either external or internal to the bell, forms the next group in an outward succession from this innermost group. A white line is manually drawn to clarify the border between particles originating from inside and outside the cavity; the X-tagged particles primarily arrive on this line. This border corresponds well with the corrugated central ridge. In other words, this ridge separates the fluid that is deflected into the wake from that which is pushed upward into the subumbrellar cavity.

In fact, the particles that have slid down the U-shaped structure depicted in the forward-time FTLE field are trapped between successive backward-time FTLE ridges. These ridges move progressively closer toward the axis of symmetry, pushing the particles with them as they move. The particles in each zone are simultaneously pulled away from the central corrugated ridge, as shown in the bottom panel of figure 7. In short, the series of forward-time FTLE ridges internal and external to the jellyfish, together with the U-shaped structure below it, represent an extended repelling LCS. The ridges

in the backward-time FTLE field, which are rooted at the corrugated central ridge, form a series of attracting LCS. These LCS complement each other to transport particles from the front of the bell into the wake, or alternatively, recirculate particles already inside the bell. The sense of this latter recirculation—upward near the central axis and downward near the subumbrellar surface of the bell—is consistent with experimental observations of live jellyfish by Dabiri *et al* [7].

4.4. FTLE fields of self-propelling versus tethered swimmers

The FTLE fields generated by the tethered system were examined and compared with those produced by the self-propelling swimmer. The forward- and backward-time FTLE fields of these cases are shown side by side in figures 11 and 12, respectively. Though the ridge patterns are qualitatively the same, there are obvious differences in the strengths of the ridges and slight differences in their placement. In particular, the series of forward-time FTLE ridges in front of the jellyfish are notably longer for the tethered case, suggesting that fluid is drawn into the wake from a larger region in this case. The larger value of the FTLE field along all ridges—both in forward- and backward-time—shows that repulsion from and attraction to the corresponding LCS are significantly faster in the tethered case.

5. Conclusions

This work has explored the use of the FTLE field for revealing Lagrangian coherent structures in low (but finite) Reynolds number biological locomotion. A new approach has been introduced for computing this FTLE field, using the data from a vortex particle simulation to induce both the particle velocities as well as the Jacobian of the flow map. The focus on the relatively simple mechanics of a self-propelling oblate jellyfish-like swimmer has allowed the flow structure to be analyzed in detail. The ridges of both the forward-and backward-time FTLE fields have been elucidated by tracking judiciously-placed groups of particles. It was shown that the ridges act as transport barriers that feed slender fingers of fluid once per cycle from the front of the jellyfish into its wake. This fluid is pulled into filaments in the wake that are revealed by the ridges of the backward-time FTLE field. Meanwhile, fluid originating inside the bell cavity apparently remains trapped in recirculation inside.

The system was also analyzed in a configuration in which the jellyfish was tethered in a steady free stream, and the FTLE field was used to highlight differences in these frames of reference. Though the flow structures are qualitatively similar, the rate of stretching in the tethered case was significantly larger along all ridges. This may have important consequences for experimental and computational studies that utilize this tethered configuration to draw conclusions about self-propelling swimmers.

References

[1] Shadden S C, Dabiri J O and Marsden J E 2006 Lagrangian analysis of fluid transport in empirical vortex ring flows *Phys. Fluids* **18** 047105

[2] Peng J and Dabiri J O 2007 A potential-flow, deformable-body model for fluid-structure interactions with compact vorticity: application to animal swimming measurements *Exp. Fluids* **43** 655–64

[3] Franco E, Pekarek D N, Peng J and Dabiri J O 2007 Geometry of unsteady fluid transport during fluid–structure interactions *J. Fluid Mech.* **589** 125–45

[4] Haller G 2001 Lagrangian structures and the rate of strain in a partition of two-dimensional turbulence *Phys. Fluids* **13** 3365–85

[5] Shadden S C, Lekien F and Marsden J E 2005 Definition and properties of Lagrangian coherent structures from finite-time Lyapunov exponents in two-dimensional aperiodic flows *Physica* D **212** 271–304

[6] Green M A, Rowley C W and Haller G 2007 Detection of Lagrangian coherent structures in three-dimensional turbulence *J. Fluid Mech.* **572** 111–20

[7] Dabiri J O, Colin S P, Costello J H and Gharib M 2005 Flow patterns generated by oblate medusan jellyfish: field measurements and laboratory analyses *J. Exp. Biol.* **208** 1257–65

[8] Eldredge J D 2007 Numerical simulation of the fluid dynamics of 2D rigid body motion with the vortex particle method *J. Comput. Phys.* **221** 626–48

[9] Eldredge J D 2008 Vorticity-based numerical simulations of dynamically coupled fluid–body interactions *J. Comput. Phys.* **227** 9170–94

[10] Eldredge J D, Colonius T and Leonard A 2002 A vortex particle method for two-dimensional compressible flow *J. Comput. Phys.* **179** 371–99

[11] Cottet G-H and Koumoutsakos P 2000 *Vortex Methods: Theory and Practice* (Cambridge: Cambridge University Press)